

Alma Mater Studiorum Università di Bologna  
Archivio istituzionale della ricerca

Mechanistic Insights into ZIF-8 Encapsulation of Atom-Precise Pt(M) Carbonyl Clusters

This is the final peer-reviewed author's accepted manuscript (postprint) of the following publication:

*Published Version:*

Kollmannsberger, K.L., Poonam, Cesari, C., Khare, R., Kratky, T., Boniface, M., et al. (2023). Mechanistic Insights into ZIF-8 Encapsulation of Atom-Precise Pt(M) Carbonyl Clusters. CHEMISTRY OF MATERIALS, 35(14), 5475-5486 [10.1021/acs.chemmater.3c00807].

*Availability:*

This version is available at: <https://hdl.handle.net/11585/938075> since: 2024-02-07

*Published:*

DOI: <http://doi.org/10.1021/acs.chemmater.3c00807>

*Terms of use:*

Some rights reserved. The terms and conditions for the reuse of this version of the manuscript are specified in the publishing policy. For all terms of use and more information see the publisher's website.

This item was downloaded from IRIS Università di Bologna (<https://cris.unibo.it/>).  
When citing, please refer to the published version.

(Article begins on next page)

This is the final peer-reviewed accepted manuscript of:

**K.L. Kollmannsberger, Poonam, C. Cesari, R. Khare, T. Kratky, M. Boniface, O. Tomanec, J. Michalicka, E. Mosconi, A. Gagliardi, S. Günther, W. Kaiser, T. Lunkenbein, S. Zacchini, J. Warnan, R. A. Fischer, "Mechanistic Insights into ZIF-8 Encapsulation of Atom-Precise Pt(M) Carbonyl Clusters", Chem. Mater., 2023, 35, 5475-5486**

The final published version is available online at:  
<https://doi.org/10.1021/acs.chemmater.3c00807>

#### Terms of use:

Some rights reserved. The terms and conditions for the reuse of this version of the manuscript are specified in the publishing policy. For all terms of use and more information see the publisher's website.

*This item was downloaded from IRIS Università di Bologna (<https://cris.unibo.it/>)*

***When citing, please refer to the published version.***

# Mechanistic insights into ZIF-8 encapsulation of atom-precise Pt(M) carbonyl clusters

*Kathrin L. Kollmannsberger, Poonam, Cristiana Cesari, Rachit Khare, Tim Kratky, Maxime Boniface, Ondřej Tomanec, Jan Michalička, Edoardo Mosconi, Alessio Gagliardi, Sebastian Günther, Waldemar Kaiser, Thomas Lunkenbein, Stefano Zacchini, Julien Warnan,\* and Roland A. Fischer\**

Kathrin L. Kollmannsberger, Tim Kratky, Sebastian Günther, Rachit Khare, Julien Warnan, Roland A. Fischer

Department of Chemistry, Technical University of Munich, Lichtenbergstraße 4, 85748, Garching, Germany

E-mail: roland.fischer@tum.de, julien.warnan@tum.de

Poonam, Alessio Gagliardi

Department Electrical and Computer Engineering, School of Computation, Information and Technology, Technical University of Munich, Hans-Piloty-Strasse 1 / III, 85748 Garching, Germany

Cristiana Cesari, Stefano Zacchini

Dipartimento di Chimica Industriale “Toso Montanari”, Università di Bologna, viale del  
Risorgimento 4, 40136 Bologna, Italy

Ondřej Tomanec

Regional Centre of Advanced Technologies and Material, Palacký University Olomouc,  
Šlechtitelů 241/27, 779 00 Olomouc, Czech Republic

Jan Michalička

Central European Institute of Technology, Brno University of Technology, Purkyňova  
123, 612 00 Brno, Czech Republic

Maxime Boniface, Thomas Lunkenbein

Department of Inorganic Chemistry, Fritz Haber Institute of the Max Planck Society,  
Faradayweg 4-6, 14195 Berlin, Germany

Edoardo Mosconi, Waldemar Kaiser

Computational Laboratory for Hybrid/Organic Photovoltaics (CLHYO), Istituto CNR di Scienze

**KEYWORDS.** carbonyl clusters, atom-precision, encapsulation, ZIF-8, host-guest

ABSTRACT. Precisely designing metal nanoparticles (NPs) is the cornerstone for maximizing their efficiency in applications like catalysis or sensor technology. Metal-organic frameworks (MOFs) with their defined and tunable pore systems provide a confined space to host and stabilize small metal NPs. In this work, the MOF encapsulation of various atom-precise clusters following the *bottle-around-ship* approach is investigated providing general insights into the scaffolding mechanism. Eleven carbonyl-stabilized Pt(M) (M = Co, Ni, Fe, Sn) clusters are employed for the encapsulation in the zeolitic imidazolate framework (ZIF)-8. Infrared and UV/Vis spectroscopy, density functional theory and *ab initio* molecular dynamics revealed structure-encapsulation relationship guidelines. Thereby, cluster polarization, size and composition, were found to condition the scaffolding behavior. Encaging of [NBnMe<sub>3</sub>]<sub>2</sub>[Co<sub>8</sub>Pt<sub>4</sub>C<sub>2</sub>(CO)<sub>24</sub>] (**Co<sub>8</sub>Pt<sub>4</sub>**) is thus achieved as the first MOF-encapsulated bimetallic carbonyl cluster, **Co<sub>8</sub>Pt<sub>4</sub>@ZIF-8**, and fully characterized including X-ray absorption near edge and extended X-ray absorption spectroscopy. ZIF-8 confinement not only promotes property changes, like the T-dependent magnetism, it further allows heat-induced ligand-stripping without altering cluster size enabling the synthesis of naked, heterometallic, close to atom-precise clusters.

## Introduction

Metal nanoparticles (NPs) composed of noble metals play a key role in many applications ranging from optics to sensors<sup>1</sup> to (electro-)catalysis<sup>2,3</sup>. The size, shape and composition of the latter determine their electronic and structural properties. The defined and target-oriented design of NPs is thereby a strategy to increase their activity.<sup>4,5</sup> To further maximize the atom-efficiency, NP downsizing is important to reach a high-density of active sites.<sup>6-8</sup> When entering the lower nanometer size regime, little changes in the atomicity can alter the NP's characteristics significantly.<sup>6,9</sup> Thus, a precisely controlled NP formula and nuclearity, down to the atomic level, is required for extracting valid structure-property relationships. As access to these defined particles still remains a huge synthetic challenge, subsequent practical investigations and understanding of nanostructured particles are difficult to reach yet.

A promising synthetic strategy for tailor-made NPs exploits metal nanoclusters (NCs) as stoichiometry-, composition- and size-defined precursors. Alternative to high-vacuum synthesis approaches, the synthesis of precise NCs can be achieved through wet conditions *via* stabilization with capping ligands.<sup>5</sup> However, the ligand shell limits the NC applicability by hampering reactant access and altering the electronic properties. Yet, ligand removal often requires harsh conditions and may lead to uncontrolled agglomeration processes.<sup>5,10</sup>

Metal-organic frameworks (MOFs) as 3D, crystalline, porous and tailorable matrixes have proven their ability to scaffold various species ranging from dyes<sup>11</sup> to metal NPs<sup>12,13</sup> to tenth of nanometer-scale enzymes<sup>14</sup>. The embedment of reactive ligand-stabilized clusters into MOFs is known, albeit rarely reported.<sup>15-21</sup> For example, [Pt<sub>9</sub>(CO)<sub>12</sub>](NBu<sub>4</sub>)<sub>2</sub> clusters were successfully encapsulated into MOF pores and enabled ligand-stripping off the cluster core to yield “naked” Pt NCs close to their original nuclearity.<sup>18</sup> The corresponding composite functioned as a template

precursor to generate small and narrow size-distributed Pt NPs ( $1.1 \pm 0.17$  nm) with high Pt mass activity for the oxygen reduction reaction.<sup>22</sup> Although the potential of scaffolding ligated atom-precise clusters with a MOF matrix is quite attractive, its mechanism and principles are hardly investigated.<sup>17,19,20</sup>

The rational *in situ* embedment of preformed guests, comprising catalytically or photoactive species like NPs, dyes or enzymes, into porous, stabilizing hosts is a fundamental goal in material chemistry.<sup>12,23</sup> Guest interfacing often grants synergistic effects like improved and long-term activity.<sup>24,25</sup> To date, reports on the latter are limited,<sup>17,20,26</sup> and lack a clear mechanistic understanding of the complex scaffolding mechanism.

Carbonyl-stabilized NCs constitute a prominent class of ligated clusters, with a wide range of nuclearity, heterogeneity, and structures, and thus represent an ideal study case toward better understanding encapsulation-structure relationships.<sup>10</sup> Herein, the *bottle-around-ship* encapsulation of a series of eleven Pt(M) (M = Co, Ni, Fe, Sn) carbonyl clusters into a zeolitic imidazolate framework (ZIF)-8 MOF is investigated including: one PtCo cluster ([NBnMe<sub>3</sub>]<sub>2</sub>[Co<sub>8</sub>Pt<sub>4</sub>C<sub>2</sub>(CO)<sub>24</sub>] (**Co<sub>8</sub>Pt<sub>4</sub>**)<sup>27</sup>), four PtNi clusters of different sizes, charges and stoichiometries ([NEt<sub>4</sub>]<sub>2</sub>[Pt<sub>5</sub>Ni(CO)<sub>12</sub>] (**Pt<sub>5</sub>Ni**)<sup>28</sup>, [NEt<sub>4</sub>]<sub>4</sub>[Pt<sub>6</sub>Ni<sub>6</sub>(CO)<sub>21</sub>] (**Pt<sub>6</sub>Ni<sub>6</sub>**), [NEt<sub>4</sub>]<sub>4</sub>[Pt<sub>16</sub>Ni<sub>3</sub>(CO)<sub>22</sub>] (**Pt<sub>16</sub>Ni<sub>3</sub>**)<sup>29</sup>, [NBu<sub>4</sub>]<sub>6</sub>[Ni<sub>35</sub>Pt<sub>9</sub>(CO)<sub>48</sub>] (**Ni<sub>35</sub>Pt<sub>9</sub>**)<sup>30</sup>), two PtFe clusters ([NEt<sub>4</sub>]<sub>2</sub>[Fe<sub>3</sub>Pt<sub>3</sub>(CO)<sub>15</sub>] (**Fe<sub>3</sub>Pt<sub>3</sub>**), [NEt<sub>4</sub>]<sub>2</sub>[Fe<sub>4</sub>Pt<sub>6</sub>(CO)<sub>22</sub>] (**Fe<sub>4</sub>Pt<sub>6</sub>**)<sup>31</sup>) and one PtSn cluster ([PPh<sub>4</sub>]<sub>4</sub>[Pt<sub>6</sub>(SnCl<sub>2</sub>)<sub>2</sub>(SnCl<sub>3</sub>)<sub>4</sub>(CO)<sub>6</sub>] (**Pt<sub>6</sub>Sn<sub>6</sub>**)<sup>32</sup>) (**Figure 1**). Further, the impact of the size effect of three different Pt clusters ([NBu<sub>4</sub>]<sub>2</sub>[Pt<sub>9</sub>(CO)<sub>18</sub>] (**Pt<sub>9</sub>**)<sup>33</sup>, [NBu<sub>4</sub>]<sub>4</sub>[Pt<sub>19</sub>(CO)<sub>22</sub>] (**Pt<sub>19</sub>**)<sup>34</sup>, [NBu<sub>4</sub>]<sub>2</sub>[Pt<sub>38</sub>(CO)<sub>44</sub>] (**Pt<sub>38</sub>**)<sup>35</sup>) was investigated. Besides featuring Pt centers, all clusters share a negatively charged core and a relative high air sensitivity. In addition, their chemical compositions in atomicity and specific bimetallic ratio may bestow high activity in (electro-

catalysis.<sup>36–39</sup> Nevertheless, despite their matching structural motifs, each cluster has unique molecule-like features as they differ in size, charge, and geometry, which may ultimately affect the encapsulation susceptibility.<sup>40,41</sup> ZIF-8 was chosen as the model scaffolding MOF due to its mild synthesis conditions, various solvent compatibility, stability, and guest size-tolerant encapsulation.<sup>14,42</sup> Further, ZIF-8 is well studied<sup>43</sup> and has proven itself applicable for NC encapsulation suitable for application.<sup>15,16,18</sup>

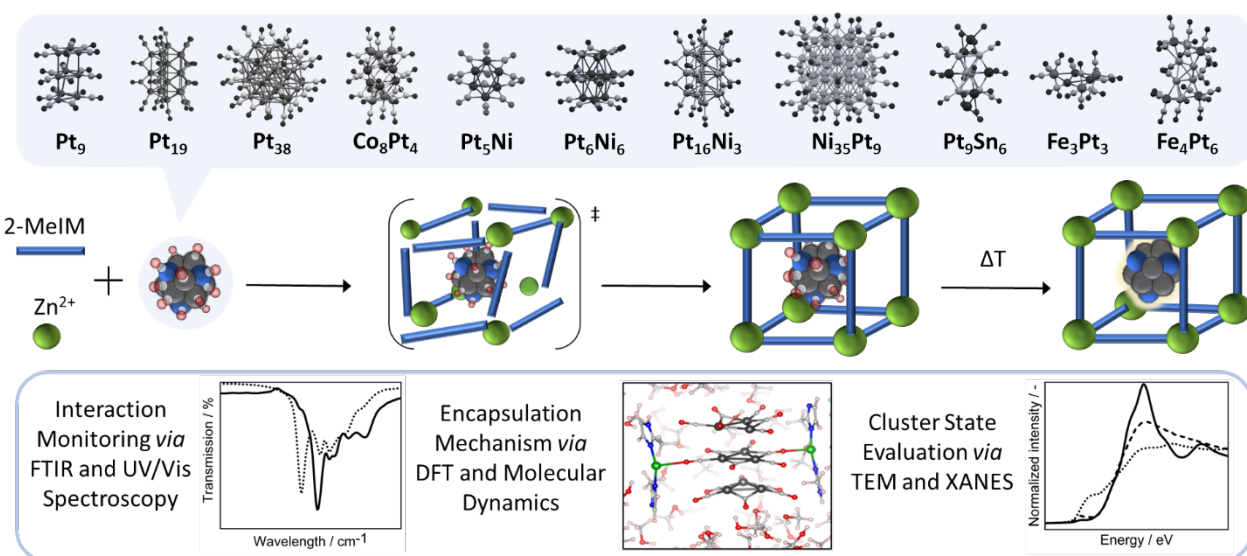


**Figure1.** Schematic overview depicting the applied CO-stabilized Pt(M) clusters in the encapsulation approach into ZIF-8. The transition state of the scaffolding process is connected to FTIR, UV/Vis spectroscopy, DFT as well as AIMD to investigate cluster and MOF building block interactions. An in-depth characterization, including TEM and XANES, renders detailed cluster status assessment within the MOF possible. The ZIF-8 confinement allows ligand removal (i.e. CO desorption) via thermal treatment, yielding the “naked” metal NCs.

Fourier-transform infrared spectroscopy (FTIR), electron microscopy, density functional theory (DFT) calculations, and *ab initio* molecular dynamics (AIMD) simulations were employed, affording insights into the encapsulation mechanism and cluster-scaffolding guidelines. After



evaluating the cluster embedment and studying the interaction mechanism of the fragile cluster and the ZIF-8 building blocks, conclusions about intrinsic encapsulation limitations, conditioned by small differences in the cluster shell polarization and cluster stability, were drawn. In-depth characterization, employing transmission electron microscopy (TEM) and X-ray absorption near edge structure (XANES) amongst others, allows to evaluate the NC integrity upon ZIF-8 embedment. Further, hand-picked cluster@MOF composites were activated yielding “naked”, pore-confined clusters (**Figure 1**). Thereby, successful embedment of **Co<sub>8</sub>Pt<sub>4</sub>** into ZIF-8 represents the first example of a bimetallic carbonyl cluster encapsulated in a MOF. Further, loading variations with a pore filling from 6 – 26 % and confinement induced physicochemical property changes were demonstrated.

## 2. Results and Discussion

### 2.1. Encapsulation of Carbonyl-Stabilized Pt(M) Clusters into ZIF-8

Literature-known procedures were used to synthesize the clusters.<sup>27–30,32,34,35,44,45</sup> Typically, the *bottle-around-ship* encapsulation into ZIF-8 was conducted by simultaneously adding cluster and linker solutions to a metal node solution under vigorous stirring at 50/60 °C in methanol (MeOH) or acetonitrile (MeCN) (details in ESI). The cluster@ZIF-8 powders are isolated after washing and drying *in vacuo*. While all experiments led to a crystalline powder ascribed to ZIF-8 from powder X-ray diffraction (PXRD) experiments (Figure S1), the success of the encapsulation procedure is determined by confirmed successful positioning of the cluster inside the MOF and the cluster integrity retention. These were evaluated by FTIR spectroscopy, diffuse reflectance (DR)-UV/Vis spectroscopy for clusters with distinct absorption bands (**Co<sub>8</sub>Pt<sub>4</sub>**, **Pt<sub>6</sub>Sn<sub>6</sub>**, **Fe<sub>4</sub>Pt<sub>6</sub>**, **Fe<sub>3</sub>Pt<sub>3</sub>**, and **Pt<sub>9</sub>**) and high angle annular dark field scanning transmission electron microscopy (HAADF-STEM) with energy dispersive X-ray (EDX) spectroscopy elemental mapping and high resolution TEM (HR-TEM).

For homometallic Pt-based clusters, FTIR spectroscopy revealed that the assembled samples display CO bands corresponding to the respective starting materials (Figure S2).<sup>18</sup> Small shifts in the CO bands are assigned to ZIF-8 induced confinement effects. Similarly, matching (DR-)UV/Vis spectra of the pristine and encapsulated **Pt<sub>9</sub>** confirmed the cluster intactness within ZIF-8 (Figure S3). HAADF-STEM with EDX elemental mapping further revealed an absence of aggregated Pt NCs which could indicate particle formation. Interestingly, **Pt<sub>19</sub>/Pt<sub>38</sub>** seems predominantly located on the edge of the ZIF-8 crystal, whereas **Pt<sub>9</sub>** is homogenously distributed (Figure S4-9).<sup>18</sup>

**Co<sub>8</sub>Pt<sub>4</sub>** cluster was effectively encapsulated into ZIF-8 from a MeOH solution yielding **Co<sub>8</sub>Pt<sub>4</sub>@ZIF-8** and clear supernatants. A close-to quantitative scaffolding for up to 0.9  $\mu\text{mol/mL}$  initial **Co<sub>8</sub>Pt<sub>4</sub>** cluster solution is anticipated. The cluster integrity was first evaluated *via* FTIR spectroscopy revealing distinct CO bands at 2033 and 1845  $\text{cm}^{-1}$  slightly offset as compared with the pristine cluster in solution (**Figure 2 a** and Figure S10 a).<sup>27</sup> The UV/Vis absorption bands of the encapsulated cluster feature a strong absorption at 685 nm in line with the pristine one (Figure 2 b). The shoulder at ~580 nm is assigned to a side species partially formed during the scaffolding process which is suspected to be a Co-2-MeIm (2-methylimidazole) due to the natural drive of Co cations to interact with 2-MeIm.<sup>46</sup> This is consistent with the UV-vis absorption of ZIF-67 as the Co(2-MeIm)<sub>2</sub>-ZIF-8 analogue (Figure S10 b).<sup>47</sup> Elemental analysis of **Co<sub>8</sub>Pt<sub>4</sub>@ZIF-8** revealed a slight Co loss of 7 mol-% in average. Competition between forming ZIF-8 and extracting Co *via* 2-MeIm coordination is likely to be the reason for the partial Co loss during the scaffolding. HR-TEM and STEM-EDX elemental mapping proved the homogenous distribution of the cluster within the ZIF-8 crystal in the absence of cluster aggregates (Figure 2 c).

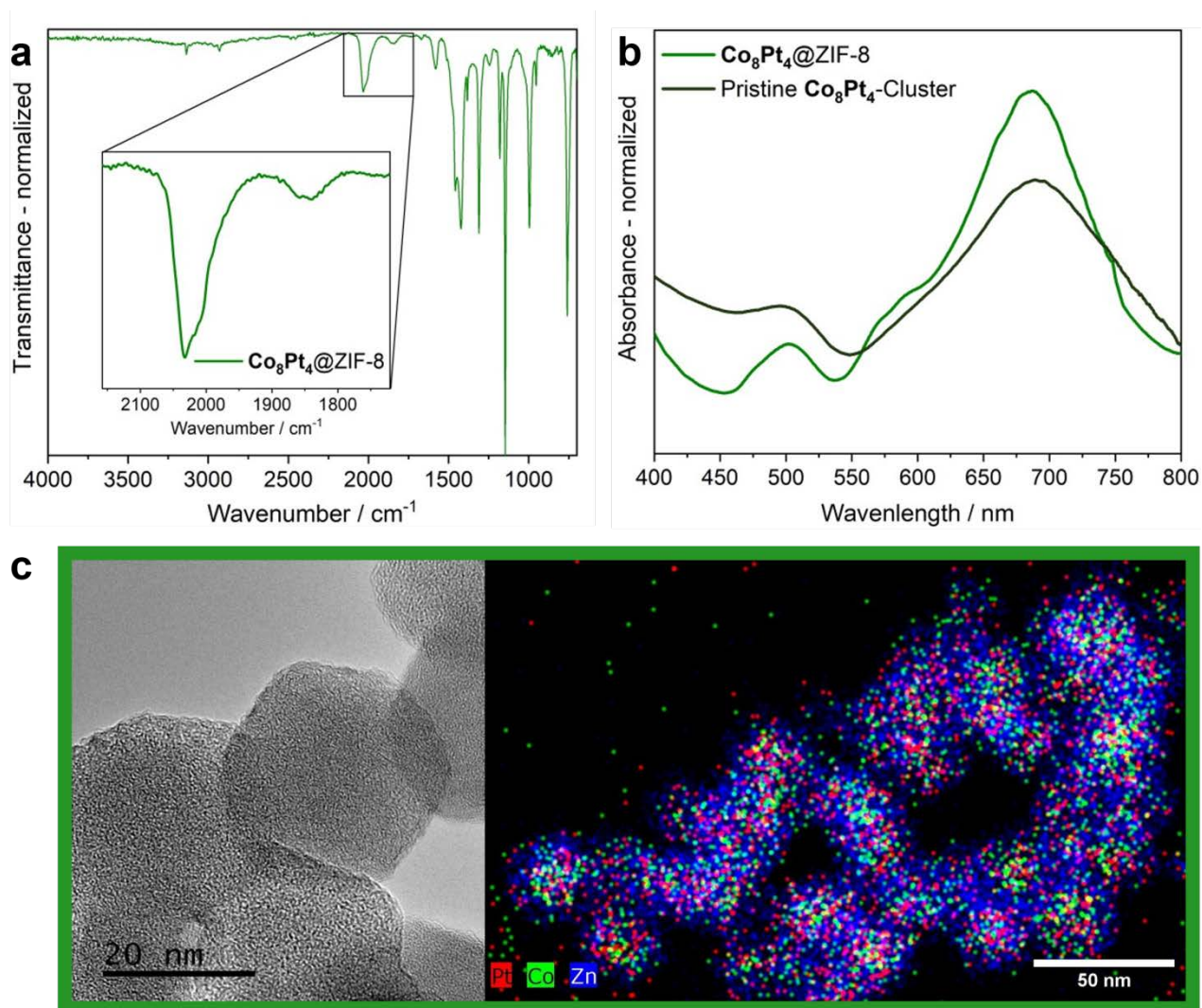


**Figure 2.** FTIR spectrum of the  $\text{Co}_8\text{Pt}_4@\text{ZIF-8}$  (a), DR-UV/Vis spectra of the pristine  $\text{Co}_8\text{Pt}_4$  cluster and encapsulated in ZIF-8 (b) and HR-TEM and STEM-EDX elemental mapping of the  $\text{Co}_8\text{Pt}_4@\text{ZIF-8}$  material (c).

The four PtNi-based clusters of the PtNi series differ in size, in Pt:Ni ratio, and in geometry. All encapsulation procedures were conducted as for the pure Pt clusters, except in MeCN at 60 °C, and afforded grey to brown powders. The IR spectra revealed no to very small CO bands (Figure S11) and elemental analysis indicated a strong enrichment of Pt content vs Ni in the cluster@ZIF-8 composites compared to the pristine clusters (Table S1). Ni leaching seems

especially pronounced for **Pt<sub>6</sub>Ni<sub>6</sub>**, unveiling Ni loss of over 90 mol-%. While successful encapsulation of the pristine cluster is also unlikely in the case of the biggest cluster (**Ni<sub>35</sub>Pt<sub>9</sub>**), HAADF-STEM revealed a predominant edge-location in the ZIF-8 crystal (Figure S12).

Pristine encapsulation of **Pt<sub>6</sub>Sn<sub>6</sub>** was unsuccessful as the dark green color of the cluster quickly turned brown during the scaffolding process, as reflected in the absorption spectra (Figure S13). Similarly, only a small CO IR band is visible of the loaded powder (Figure S14) and the elemental analysis revealed a Sn loss of about 20%.

Encapsulation attempts of either **Pt<sub>3</sub>Fe<sub>3</sub>** or **Pt<sub>4</sub>Fe<sub>6</sub>** lead to ZIF-8 precipitation as a white powder while the colored cluster solution and corresponding supernatant UV/Vis absorption remained unaltered (Figure S15 and S16). The IR spectra of the precipitate confirmed the lack of cluster incorporation as the CO bands are absent (Figure S17) and elemental analysis showed insignificant amounts of Fe and Pt.

The supporting ability of ZIF-8 matrix was further evaluated *via* comparison with an impregnation approach where **Pt<sub>9</sub>** or **Co<sub>8</sub>Pt<sub>4</sub>** (as representative examples) and preformed ZIF-8 particles were placed together in solution. Exposing **Pt<sub>9</sub>** to ZIF-8 particles resulted in cluster alteration as seen by the disappearance of the characteristic absorption bands (Figure S3). This matches our expectations as solubilized **Pt<sub>9</sub>** is already altered in the presence of the either the metal node or the linker (*cf.* Figure S21). The DR-UV/Vis and FTIR spectra of the impregnated **Co<sub>8</sub>Pt<sub>4</sub>/ZIF-8** revealed cluster features matching with those of the pristine cluster (Figure S18). As CO band shifts would indicate strong cluster-support interactions,<sup>48</sup> here, poor **Co<sub>8</sub>Pt<sub>4</sub>-ZIF-8** interactions are anticipated. After MeOH washing of **Co<sub>8</sub>Pt<sub>4</sub>/ZIF-8** cluster-based features were no longer detectable in the isolated powder (Figure S18). This shows the successful 3D pore-confinement and the superior stabilizing impact of the encapsulation approach.

The scaffolding process outcome (summarized in Figure S19) suggest direct correlations with the structure of the cluster. The local distribution of the clusters within the ZIF-8 crystal can be correlated with the cluster size. **Pt<sub>9</sub>** matches the cavity-size ( $d_{\text{max,Pt9}} = 7.12 \text{ \AA}$ ,  $d_{\text{ZIF-8pore}} = 11.6 \text{ \AA}$ , *cf.* Table S2 summarizing the cluster sizes) and is distributed homogeneously throughout the ZIF-8 crystal. Conversely, bigger clusters such as **Pt<sub>38</sub>**, **Pt<sub>19</sub>** and **Ni<sub>35</sub>Pt<sub>9</sub>** locate at the edge of the crystals. Despite the ability of ZIF-8 to host pore-size-exceeding guests, the driving force is assumed to be lower as defects must be included in the matrix, suggesting that cavity-size matching is anticipated to promote homogeneously distributed clusters.<sup>49</sup> In the case of heterometallic clusters, Pt-M bond energy is likely a key factor as the comparably weak Pt-Sn<sup>50</sup> and Pt-Ni bonds<sup>10</sup> did not withstand the reaction conditions resulting in cluster alteration and Sn/Ni leaching, albeit partial cluster preservation may occur as in some cases. An interstitial carbide moiety<sup>51</sup> and structural effects, including ligand shielding and a particular electronic structure,<sup>52</sup> promote the stability of **Co<sub>8</sub>Pt<sub>4</sub>** and PtFe clusters, respectively. However, while **Co<sub>8</sub>Pt<sub>4</sub>** and PtFe clusters were able to withstand the reaction conditions overall, only the former enabled a successful cluster@ZIF-8 formation. Yet, these correlations fail to provide across the board insights toward defining structure(/composition)-encapsulation relationship and guiding principles.

## 2.2 Cluster-Encapsulation Relationship

While not fully understood, successful encapsulation is commonly associated with suitable guest–MOF building block interactions.<sup>17,53</sup> To first assess this, we investigated the impact of each ZIF-8 building block on the cluster's stability by exposing the cluster solutions (~890  $\mu\text{M}$ ) to  $\text{Zn}^{2+}$  (53 mM) or to 2-MeIm (263 mM). The solutions were directly analyzed *via* liquid cell FTIR spectroscopy, monitoring changes in the characteristic CO bands (Figure S20), and UV/Vis

spectroscopy for tracking color changes (Figure S2**1**). Table S3 summarizes the trends of the cluster-building block interactions.

Upon exposure to  $\text{Zn}^{2+}$  cations, seven (**Pt<sub>5</sub>Ni**, **Pt<sub>6</sub>Ni<sub>6</sub>**, **Pt<sub>16</sub>Ni<sub>3</sub>**, **Ni<sub>35</sub>Pt<sub>9</sub>**, **Fe<sub>3</sub>Pt<sub>3</sub>**, **Pt<sub>9</sub>**, and **Pt<sub>19</sub>**) out of eleven clusters show a distinct CO band shift in the IR spectra toward higher wavenumbers while three clusters (**Co<sub>8</sub>Pt<sub>4</sub>**, **Fe<sub>4</sub>Pt<sub>6</sub>**, **Pt<sub>38</sub>**) remain unaffected (see Figure S2**0**). CO band shifts are not necessarily associated with cluster structure alteration but rather with electron density changes upon the interaction of the probe molecules. Higher wavenumbers suggest significant interactions between  $\text{Zn}^{2+}$  and the negatively charged clusters leading to a reduced electron density in the CO-M bond rendering the  $\pi$ -back bonding weaker and, thus, the CO bond stronger and less polarized.<sup>54</sup> The reactivity of small carbonyl platinum clusters toward  $\text{Zn}^{2+}$  is in accordance with prior literature reporting interaction with electrophiles.<sup>45</sup> In the case of **Pt<sub>6</sub>Sn<sub>6</sub>** and **Pt<sub>6</sub>Ni<sub>6</sub>**, precipitation from the media and lower intensity CO band suggest degradation of the cluster. Similarly, **Fe<sub>3</sub>Pt<sub>3</sub>** and **Pt<sub>9</sub>** change color in the presence of  $\text{Zn}^{2+}$  as **Pt<sub>9</sub>** likely transforms to  $[\text{Pt}_{15}(\text{CO})_{30}]^{2-}$  in accordance with prior reports (Figure S2**1c, d**).<sup>55</sup>

Upon exposure to 2-MeIm, **Co<sub>8</sub>Pt<sub>4</sub>**, **Pt<sub>5</sub>Ni**, **Pt<sub>6</sub>Ni<sub>6</sub>**, **Pt<sub>16</sub>Ni<sub>3</sub>**, **Fe<sub>4</sub>Pt<sub>6</sub>**, **Fe<sub>3</sub>Pt<sub>3</sub>**, and **Pt<sub>19</sub>** reveal no distinct CO-band shifts whereas clusters with a higher nuclearity, **Ni<sub>35</sub>Pt<sub>9</sub>** and **Pt<sub>38</sub>**, display a shift to lower wavenumbers. High nuclearity clusters have been reported to interact with nucleophiles acting as a Lewis base transferring electron density to the clusters *via* coordination.<sup>45</sup> For the smaller clusters **Pt<sub>9</sub>** and **Pt<sub>6</sub>Sn<sub>6</sub>** that display a shift and a strong decrease in CO-band intensity, respectively, the changes are in line with a transformation to higher Pt nuclearity<sup>34</sup> and degradation, respectively. These trends are also observed in the corresponding UV/Vis spectra with **Pt<sub>9</sub>**, **Pt<sub>6</sub>Sn<sub>6</sub>** displaying significant changes while **Fe<sub>3</sub>Pt<sub>3</sub>** and **Co<sub>8</sub>Pt<sub>4</sub>** remaining relatively unaltered (Figure S2**1**). In the case of **Co<sub>8</sub>Pt<sub>4</sub>**, while overall unchanged, the emerging shoulder at

~584 nm in the DR-UV/Vis spectra (Figure 2 b) prompted us to conduct further stability tests at higher temperatures with heating to > 50 °C leading to cluster decomposition presumably from the formation of a Co(2-MeIm)<sub>2</sub>-type complex (Figure S22).<sup>56</sup>

Summarizing this stability study, IR and UV/Vis spectra provide decisive qualitative information about the cluster-building block interactions and thermodynamic products. We found that **Pt<sub>6</sub>Ni<sub>6</sub>**, **Pt<sub>6</sub>Sn<sub>6</sub>**, **Fe<sub>3</sub>Pt<sub>3</sub>**, and **Pt<sub>9</sub>** are not tolerant to the individual building blocks and all PtNi clusters lose Ni in the scaffolding process (*cf.* 2.1). Nevertheless, caution must be exercised in the assessment of a given cluster's potential for encapsulation. For instance, although **Pt<sub>9</sub>** is altered in the presence of Zn/2-MeIm, unscathed entrapment has been reported owing to fast ZIF-8 crystallization kinetics.<sup>18</sup> While the lack of stability of some clusters may account for the unsuccessful encapsulation, it only partially explains the encapsulation results as, for instance, Fe clusters appear tolerant yet unencapsulated.

Next, we simulated the nucleation environment by computing the chemical interactions of ZIF-8 precursors with **Pt<sub>9</sub>**, **Pt<sub>3</sub>Fe<sub>3</sub>**, and **Co<sub>8</sub>Pt<sub>4</sub>** clusters from DFT (*cf.* ESI). These were selected as representative candidates for their stability in the reaction conditions yet discrepancies in their encapsulation outcome.

[Zn(2-MeIm)<sub>*n*</sub>]<sup>2+</sup> moieties (*n* = 0-3, number of 2-MeIm linkers; as shown in Figure S23) - representative of the early stages of ZIF-8 nucleation - are placed such that the Zn center bonds at the carbonyl ligands or at the metal centers of the Pt(M) clusters, with detailed representations shown in Figures S24 to S26. The interaction between [Zn(2-MeIm)<sub>*n*</sub>]<sup>2+</sup> and the clusters is characterized by the adsorption energy:

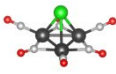
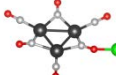
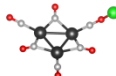
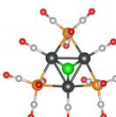
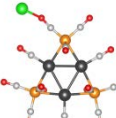
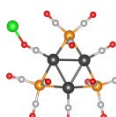
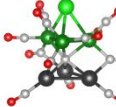
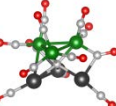
$$E_{\text{ads}} = E(\text{Zn(2-MeIm)+cluster}) - E(\text{Zn(2-MeIm)}) - E(\text{cluster})$$

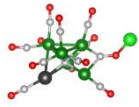
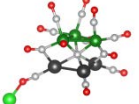
where  $E(\text{cluster})$  is the energy of the isolated Pt(M) cluster,  $E(\text{Zn(2-MeIm)})$  gives the energy of the  $[\text{Zn(2-MeIm)}_n]^{2+}$  complex, and  $E(\text{Zn(2-MeIm)+cluster})$  gives the energy of the  $[\text{Zn(2-MeIm)}_n]^{2+}$  complex bonded to the Pt(M)-cluster. Note that solvent effects are included in the CPCM model, see ESI. **Table 1** summarizes the adsorption energies  $E_{\text{ads}}$  for the most relevant adsorption sites with  $n = 0$  to 2 cross-linkers (please see Tables S4-6 for all adsorption energies at all sites and  $n = 3$  data).

For **Pt<sub>9</sub>**, we observe substantial binding of the  $[\text{Zn(2-MeIm)}_n]^{2+}$  complex for  $n < 3$  at site 1 due to the formation of Zn-Pt bonds at the exposed Pt atoms in the outer layer. Less strong formation energies are observed for CO at sites 2 and 3, representing a bridged and a terminal position, respectively. Still, a clearly enhanced attraction of the precursor complex at the bridged carbonyl ligand is observable, with nearly twice as large adsorption energies and a reduced distance between the Zn center and the O atom of the ligand (see Figures S27 and S28). With an increased amount of (2-MeIm) linkers  $n$ ,  $E_{\text{ads}}$  decreases and the distance between the Zn center and the cluster increases due to a steric hindrance to form Zn-O bonds. The latter observation may be important in the later stages of the MOF formation, where the cross-linking between the  $\text{Zn}^{2+}$  ions occurs in the surrounding of the Pt clusters and requires desorption of  $[\text{Zn(2-MeIm)}_n]^{2+}$  from the carbonyl ligands. The C-O bond of terminal carbonyl ligands ( $\sim 1.20\text{-}1.21$  Å) is slightly shorter than the one of the bridged CO ligands ( $\sim 1.24\text{-}1.25$  Å), underlining the greater back-bonding in the bridged carbonyl ligands.<sup>57</sup> Consequently, O atoms of terminal ligands have a reduced charge density compared to the ones of bridged ligands, hampering the attraction of the positively charged  $\text{Zn}^{2+}$  ions.



**Table 1.** Adsorption energies  $E_{\text{ads}}$  of the ZIF-8 precursors  $[\text{Zn}(\text{2-MeIm})_n]^{2+}$  with  $n$  (2-MeIm) cross-linkers at chemically distinct sites of **Pt<sub>9</sub>**, **Pt<sub>3</sub>Fe<sub>3</sub>**, and **Co<sub>8</sub>Pt<sub>4</sub>**. All values are given in units of eV. A simplified representation of the adsorption sites is given for each site. Please refer to Figures S24 to S26 and Tables S4 to S6 for detailed visualization of the adsorption sites and all calculated adsorption energies, respectively. The color scheme used: C (light grey); O (red); Zn (green); Pt (dark grey); Fe (orange); Co (dark green).

Cluster	Site #	Representation	$\text{Zn}^{2+}$	$[\text{Zn}(\text{2-MeIm})_1]^{2+}$	$[\text{Zn}(\text{2-MeIm})_2]^{2+}$
<b>Pt<sub>9</sub></b>	1		−3.001	−2.331	−1.507
	2		−0.997	−0.935	−0.557
	3		−0.585	−0.469	−0.348
<b>Pt<sub>3</sub>Fe<sub>3</sub></b>	1		−2.485	−1.082	−0.548
	2		−0.637	−0.585	−0.449
	3		−0.723	−0.659	−0.345
<b>Co<sub>8</sub>Pt<sub>4</sub></b>	1		−1.213	−0.707	−0.409
	2		−0.836	−0.780	−0.521

3		-0.573	-0.474	-0.329
4		-0.960	-0.827	-0.547
5		-0.467	-0.418	-0.296

---

For **Pt<sub>3</sub>Fe<sub>3</sub>**, the largest interaction is again observed at the “upper” site 1 due to Zn-Pt bonds, which is followed by site 3, indicating a terminal CO-ligand bonded to Fe, and site 2, a terminal CO ligand bonded to Pt. Interestingly, the interaction of the  $[\text{Zn}(\text{2-MeIm})_n]^{2+}$  complexes with the metal atoms drops more rapidly with increasing  $n$  compared to the **Pt<sub>9</sub>** cluster, which is due to the vertical carbonyl ligands reducing the space to bind the Zn ion to the Pt metal center. For **Co<sub>8</sub>Pt<sub>4</sub>**, we observed values for the adsorption at carbonyl ligands that are comparable to those of the **Pt<sub>9</sub>** cluster. Comparing **Pt<sub>9</sub>**, **Co<sub>8</sub>Pt<sub>4</sub>** and **Pt<sub>3</sub>Fe<sub>3</sub>**, bridging carbonyl ligands show the strongest binding compared to all terminal CO ligands independent of the coordinating metal. In contrast to **Pt<sub>9</sub>** and **Pt<sub>3</sub>Fe<sub>3</sub>**, all “upper” metal atoms of **Co<sub>8</sub>Pt<sub>4</sub>** are terminated with vertical carbonyl ligands which strongly reduces the bond formation of Zn ions with metal centers at site 1. The latter observation may explain the CO-band shift in the IR spectra for **Pt<sub>9</sub>** and **Pt<sub>3</sub>Fe<sub>3</sub>** upon adding  $\text{Zn}(\text{NO}_3)_2$ , which is unobserved for **Co<sub>8</sub>Pt<sub>4</sub>** (see Figure S20).

To assure successful encapsulation, it is necessary to create a  $[\text{Zn}(\text{2-MeIm})_n]^{2+}$  rich environment around the Pt(M) clusters. As shown from DFT calculations, metal sites as well as both terminal and bridged carbonyl ligands reveal an attractive interaction with the ZIF-8

precursors. However, the encapsulation process occurs in solution, and competition between solvation of  $[\text{Zn}(\text{2-MeIm})_n]^{2+}$  complexes and adsorption at the Pt(M) clusters needs further understanding. To rationalize this competition, we performed AIMD simulations in a MeOH solution (see Figure S29 for structural models) on **Pt<sub>9</sub>** and **Pt<sub>3</sub>Fe<sub>3</sub>** only to limit computational time. Here, two  $[\text{Zn}(\text{2-MeIm})_2]^+$  precursor complexes were positioned at distinct CO ligand sites: (i) for **Pt<sub>9</sub>**, one complex is placed at the bridged CO ligand – labeled as Zn(1) – and one is placed at the terminal CO ligand – labeled as Zn(2); (ii) for **Pt<sub>3</sub>Fe<sub>3</sub>**, we placed one precursor complex at the Fe-bonded CO ligand – labeled as Zn(1) – and the other one at the Pt-bonded CO ligand – labeled as Zn(2). Note that we have deprotonated one 2-MeIm molecule to keep the supercell in a charge-neutral state. A detailed description of the model setup and computational details are given in the ESI.

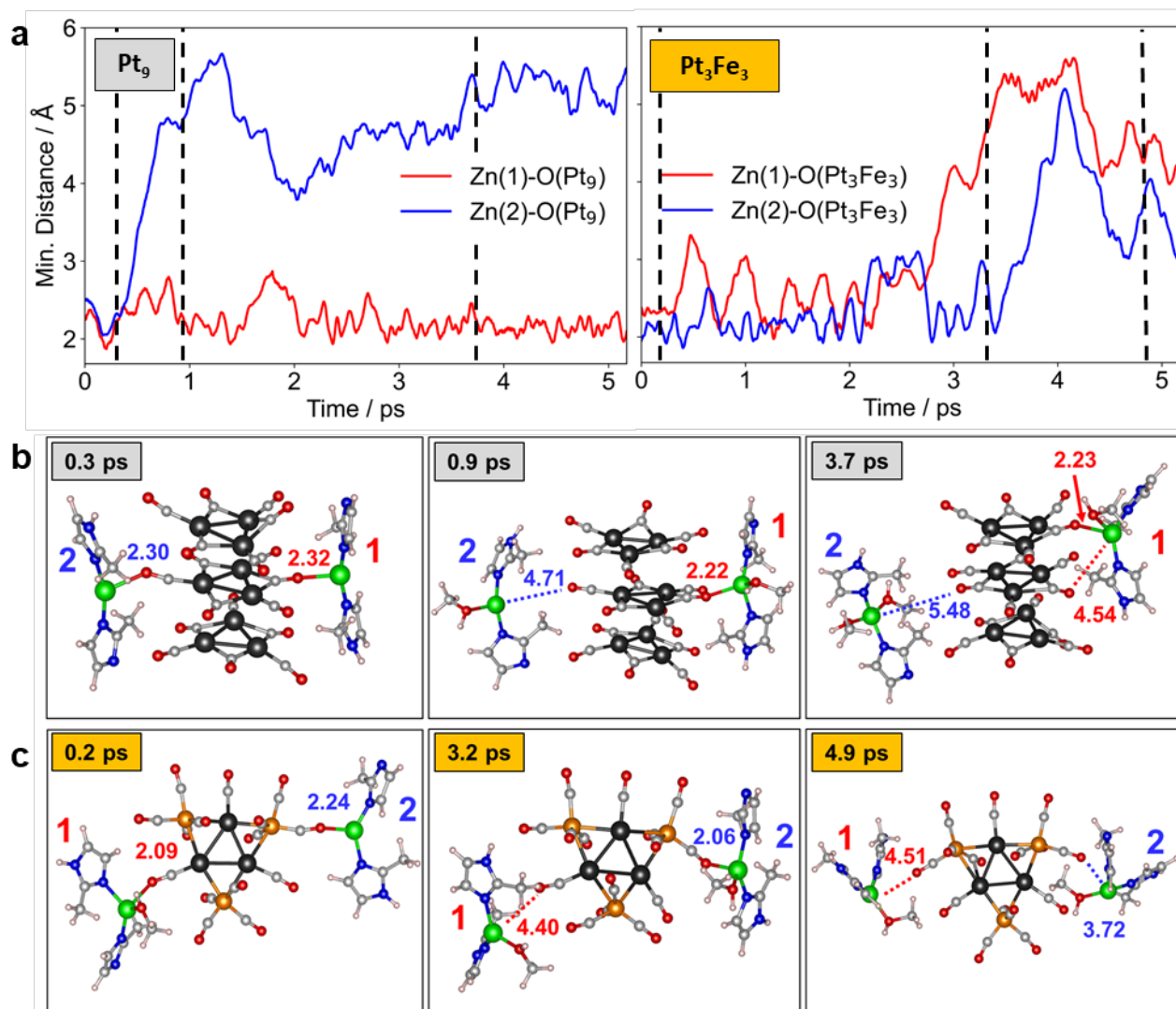


**Figure 3.** Structural evolution of the ZIF-8 precursor complexes in a MeOH solution for **Pt<sub>9</sub>** and **Pt<sub>3</sub>Fe<sub>3</sub>** clusters from AIMD. **a** Time evolution of the distance between Zn<sup>2+</sup> ions and the nearest O atom of the (left) **Pt<sub>9</sub>** and (right) **Pt<sub>3</sub>Fe<sub>3</sub>** cluster. Snapshots in **b** and **c** visualize important steps in the adsorption/desorption process in the **Pt<sub>9</sub>** and **Pt<sub>3</sub>Fe<sub>3</sub>** cluster, respectively. For improved readability, solvent molecules are only visualized if bonding to the Zn<sup>2+</sup> ions. Zn atoms are labeled consistently to guide the reader's eye; characteristic distances between Zn and the nearest CO ligands are labeled at each Zn atom. The colors of the atoms are as follows: Pt (dark grey); Fe (orange); O (red); C (light grey); Zn (green); N (blue); H (white).

For the **Pt<sub>9</sub>** cluster, we observed substantial differences in the time evolution of the distance, given by the minimum distance between Zn and O cluster atoms, see **Figure 3 a** for the time evolution and **Figure 3b** for characteristic snapshots. The Zn(1) ion, initially bonded to a bridged carbonyl ligand, remains bonded to the cluster as indicated by the short minimum distance throughout the trajectory. Zn(2), initially bonded to a terminal carbonyl ligand, shows a rapid increase in distance to the cluster at ~0.5 ps to values above 4 Å, suggesting facile desorption of Zn ions from terminal CO ligands. At ~0.35 ps, MeOH molecules bind with both Zn ions as seen in the increase in the Zn/O(MeOH) coordination number, see **Figure S30** and a snapshot at 0.9 ps. The binding of MeOH reduces the bond strength between the Zn ions and the cluster, which eventually is sufficient to cause the Zn(2) desorption from the cluster, see **Figure 3b**. At 1.2 ps, a second MeOH binds to the desorbed Zn(2) and remains bonded throughout the trajectory (snapshot at 3.7 ps in **Figure 3b** and **Figure S30 a**). The additional MeOH stabilizes the precursor complex in the MeOH solution and fully suppresses the interaction with **Pt<sub>9</sub>**. For Zn(1), around one MeOH molecule remains bonded; still, Zn(1) keeps the bond to **Pt<sub>9</sub>**, which supports the stronger interaction with bridged carbonyl ligands as proposed from our DFT calculations. Interestingly, at 1.7 ps the ZIF precursor complex migrates from the bridged ligand at the central Pt layer to the bridged ligand at the upper Pt layer, see snapshot at 3.7 ps in **Figure 3b**. The Zn(1) bond to the central and upper bridged CO remains stable throughout the remaining simulation time, which points to an additional stabilization of the precursor at the cluster due to reduced steric hindrance (**Figure S31**).

For the **Pt<sub>3</sub>Fe<sub>3</sub>** cluster, both Zn ions remain bonded to the cluster throughout the first 3 ps of simulation time, while large fluctuations in the Zn-O distances point to a strong competition between binding at the cluster and solvation by MeOH, which are coordinated to the Zn ions

(cf. Figure S30). At 2.9 ps, the distance between Zn(1) and the cluster rapidly increases beyond 4 Å (Figure 3a and Figure 3c), demonstrating the desorption of Zn(1) from the cluster. Further desorption of Zn(2) is observed at 3.6 ps, shown by the distance increase up to values of 3.5 Å. Interestingly, the timescales during which the Zn ions remain bonded to the Pt(M) clusters follow the adsorption energy from DFT calculations, showing a decrease in the order **Pt<sub>9</sub>**(bridged) > **Pt<sub>3</sub>Fe<sub>3</sub>** (terminal at Fe) > **Pt<sub>3</sub>Fe<sub>3</sub>** (terminal at Pt) > **Pt<sub>9</sub>**(terminal).

Based on the theoretical and experimental observations, we may hypothesize criteria that must be fulfilled to allow for the successful encapsulation of Pt(M) clusters inside the ZIF-8. Firstly, the clusters require sufficient stability. Thus, pure Pt clusters, which are more stable, can be easier scaffolded intactly, whereas Pt-M clusters with weaker intermetallic bonds (e.g., M = Ni, Sn) tend to lose most of the non-noble metal during the MOF formation. Secondly, bigger clusters remain rather located on the crystal edge. Thirdly, the negative cluster charge itself is not sufficient to permit successful scaffolding (e.g., case of the **Pt<sub>3</sub>Fe<sub>3</sub>** cluster) and we found that the polarization of the carbonyl ligands likely plays a pivotal role in the encapsulation process. In particular, bridged carbonyl ligands show enhanced attraction of the ZIF-8 precursor ions in contrast to terminal carbonyl ligands. This likely creates a ZIF-8 precursor-rich environment around the clusters even in the intermediate stage of the crystal growth. This may be considered as the key to the successful encapsulation as larger distances between clusters and MOF precursors (i.e., weaker precursor-cluster interactions) coincide with exclusion of the cluster from the MOF growth.

### 2.3 Characterization and Activation of Co<sub>8</sub>Pt<sub>4</sub>@ZIF-8

The **Co<sub>8</sub>Pt<sub>4</sub>** cluster exemplifies the reachability of scaffolding atom-precise bimetallic clusters into ZIF-8 without losing overall their original structure. Next, we exploited this achievement by conducting an in-depth investigation of the conditioning of the cluster into **Co<sub>8</sub>Pt<sub>4</sub>@ZIF-8** composite and its activation *via* ligand removal.

First, following the cluster's encapsulation, a thorough investigation of the **Co<sub>8</sub>Pt<sub>4</sub>@ZIF-8** material was conducted. Upon dissolving the MOF in an acidic solution (0.1 M AcOH in MeOH), electrospray ionization mass spectrometry (ESI-MS) revealed a comparable isotope pattern as obtained for the pristine **Co<sub>8</sub>Pt<sub>4</sub>** (Figure S32), with a preserved cluster core visible as  $[\text{Co}_8\text{Pt}_4\text{C}_2(\text{CO})_{24-x}]^z$  ( $z = -2$ ,  $x = 5$  to  $8$ ;  $z = -1$ ,  $x = 0$  to  $5$ ). The observation of partial CO loss and different cluster charges ( $z = -1/-2$ ) can be explained by the ionization process and by partial cluster oxidation.<sup>28</sup> For the MOF-extracted cluster, the CO loss can originate from the encapsulation process as **Co<sub>8</sub>Pt<sub>4</sub>** has a diameter which slightly exceeds the maximum pore size (11.9 vs 11.6 Å). The digestion solution was analyzed *via* UV/Vis spectroscopy revealing matching absorption bands (Figure S33). Both methods confirm the presence of intact clusters outside, after MOF digestion, and consequently inside ZIF-8.<sup>17</sup>

X-ray photoelectron spectroscopy (XPS) measurements show characteristic Zn 2p and N 1s core level spectra for ZIF-8<sup>58,59</sup> as well as metallic Pt 4f signals (71.1 eV) while distinct Co signals are absent (Figure S34). Due to the higher kinetic energy of Pt 4f photoelectrons (~1180 eV) compared to 2p Co photoelectrons (~230 eV), the latter show a higher surface sensitivity than the former because of a decreased signal attenuation length. Thus, complete **Co<sub>8</sub>Pt<sub>4</sub>** scaffolding is anticipated, with the ZIF-8 matrix hindering the low-energy Co 2p photoelectrons from escaping.

Next, we examined the XANES of ZIF-8-hosted cluster at the Co-K absorption edge. Comparison between the pristine cluster, Co-foil, and Co(II) oxide inferred that the pure **Co<sub>8</sub>Pt<sub>4</sub>** cluster holds characteristics pertaining to partially oxidized Co (**Figure 4 a**). Upon encapsulation into the MOF structure, further oxidation of the **Co<sub>8</sub>Pt<sub>4</sub>** clusters was observed, which could stem from the interaction with the ZIF-8 matrix, partial removal of CO ligands, and also from X-ray beam damage during the measurement.

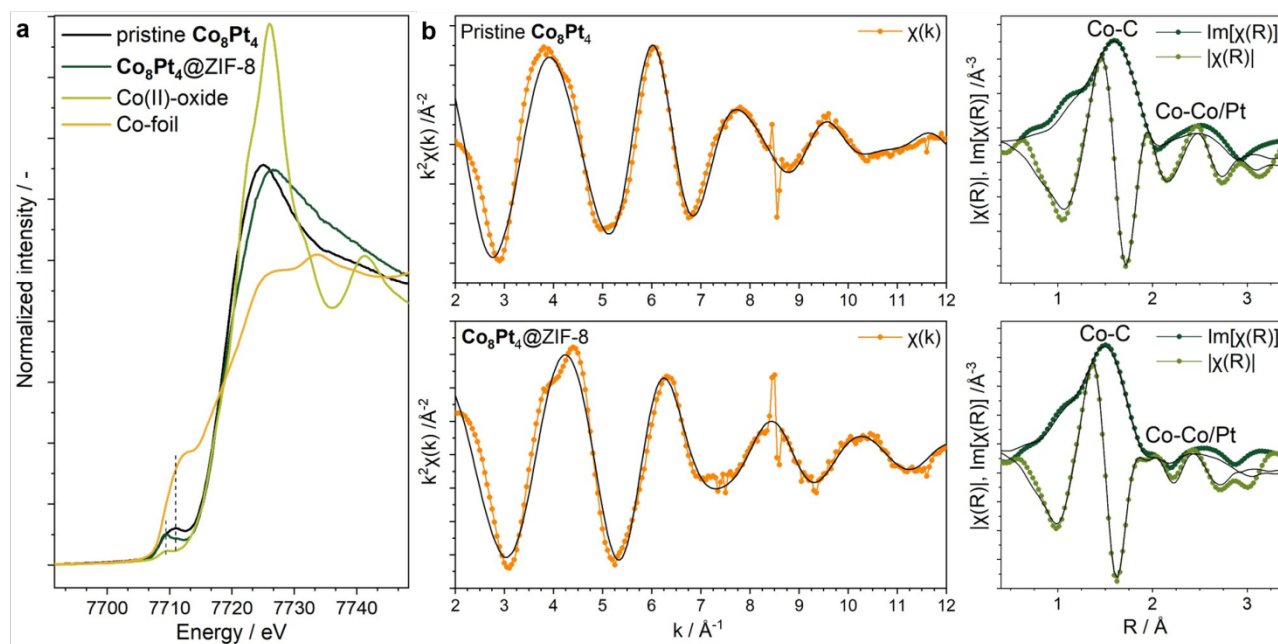


**Figure 4.a** Co K-edge XANES of **Co<sub>8</sub>Pt<sub>4</sub>** clusters, **Co<sub>8</sub>Pt<sub>4</sub>@ZIF-8**, Co-foil and Co(II)-oxide. **b**  $k^2$ -weighted EXAFS (left) and Fourier-transformed EXAFS (right) of the pure **Co<sub>8</sub>Pt<sub>4</sub>** cluster (top) and **Co<sub>8</sub>Pt<sub>4</sub>@ZIF-8** (bottom).

Extended X-ray absorption fine structure (EXAFS) measurements allowed to gain more insights into the structure of **Co<sub>8</sub>Pt<sub>4</sub>** clusters inside the MOF pore and the impact of the entrapment. Figure 4b depicts the EXAFS and Fourier transformed (FT)-EXAFS of pure **Co<sub>8</sub>Pt<sub>4</sub>** clusters and **Co<sub>8</sub>Pt<sub>4</sub>@ZIF-8**. The corresponding EXAFS fitting parameters are presented in Table S7, including the theoretical average coordination numbers (CN) and the corresponding



interatomic distances (d). The EXAFS of the as-prepared **Co<sub>8</sub>Pt<sub>4</sub>** clusters matched closely the theoretically predicted CNs and interatomic distances. Upon cluster scaffolding, a decrease in interatomic distances is recorded (e.g.,  $d_{\text{Co-Co}}$  decreased from  $\sim 2.1$  Å in the pristine to  $\sim 2.0$  Å in the encapsulated **Co<sub>8</sub>Pt<sub>4</sub>**), suggesting that the cluster is constricted within the micropores of the framework. This indicates, besides the cluster core retainment, distinct MOF-induced cluster confinement, which is known to affect the clusters' physicochemical properties.<sup>60,61</sup>

Here, the effect on the paramagnetic properties of the MOF-hosted **Co<sub>8</sub>Pt<sub>4</sub>** were evaluated by superconducting quantum interferometer device (SQUID) measurements.<sup>62</sup> The linear magnetization vs the magnetic field strength, as well as the preservation of the positive magnetization until 110 K, confirmed the overall paramagnetic behavior of the **Co<sub>8</sub>Pt<sub>4</sub>@ZIF-8** (Figure S35). At lower temperatures ( $< 110$  K) the material becomes solely diamagnetic. This contrasts with the behavior of the pristine cluster as a prior report suggested that 25% of the clusters are in a  $S = 1$  ground state at 2 K and that the spin population in the ground state is influenced by local deformations leading to spin-crossover.<sup>62</sup> Here the encapsulation seems to change the T dependence of the phenomena yielding a population of solely  $S = 0$  state below 100 K. This can be ascribed to the MOF confinement likely inducing strains on the clusters which in turn alter the relative  $S = 1$  and  $S = 0$  population magnetic states.

Finally, we investigated the cluster loading capacity and its influence on the framework crystallinity, porosity, and stability to understand and define the materials' limitations with the respective properties. Here, the one-pot synthesis enabled cluster loading from 1.2 to 5.3 wt.-% Pt with a pore filling of 6 – 26 %, respectively, simply by increasing the initial cluster equivalent (from 0.002 to 0.016 eq.) in the reaction media. The differently loaded networks show high crystallinity (Figure S36) while Brunauer-Emmett-Teller (BET) surface areas linearly decrease

with cluster loading due to the increased amount of non-porous material (Figure S37 a). The respective N<sub>2</sub> adsorption isotherms revealed hysteresis in the microporous regime, which shrinks and shifts with increased loadings coinciding with a decreased MOF flexibility due to the pore filling and related crystal defects (Figure S37 b, c).<sup>63</sup> The latter is also inferred by the corresponding thermogravimetric analysis (TGA) demonstrating high thermal stability with a slight decrease in the decomposition temperature (from ~535 to 485 °C) at higher loadings (Figure S38). DR-UV/Vis and FTIR spectroscopy further reflected the various cluster amounts embedded in ZIF-8 based on respective intensity changes (Figure S39). Even though one quarter of the pores can be filled with clusters, the properties of the highly porous and stable material were preserved.

Secondly, the three-dimensional stabilization allows to remove the CO ligands to obtain a bare CoPt cluster, electronically and sterically not influenced by a surfactant shell, without facing agglomeration. To activate the CoPt clusters inside ZIF-8 a ligand stripping procedure was conducted as heat treatment (HT) at 200 °C under a dynamic vacuum yielding Co<sub>8±x</sub>Pt<sub>4±y</sub>NC@ZIF-8. PXRD (Figure S40a) spectra of the activated samples revealed retention of the MOF crystallinity. The activation procedure was monitored *via* temperature programmed desorption (TPD, 26 °C/min) coupled with quadrupole mass spectrometry (QMS) in ultra-high vacuum (UHV) in the XPS. A distinct CO signal (m/z 28) is visible in the mass analysis (**Figure 5 a**) starting off at 60 °C and diminishes already at 190 °C and which is over 8 times higher relative to the trace water signal. Comparing IR spectra before and after the HT (Figure 5b) further evidenced complete CO ligand removal. Interestingly, this ligand stripping step was not accompanied by agglomeration of the newly-formed highly reactive naked clusters as HR-TEM images point toward core preservation or undetected minor nuclearity changes (Figure 5 c and

Figure S40b). This is in line with the XPS spectra before and after the 200 °C HT displaying no distinct signal alterations (Figure S34).

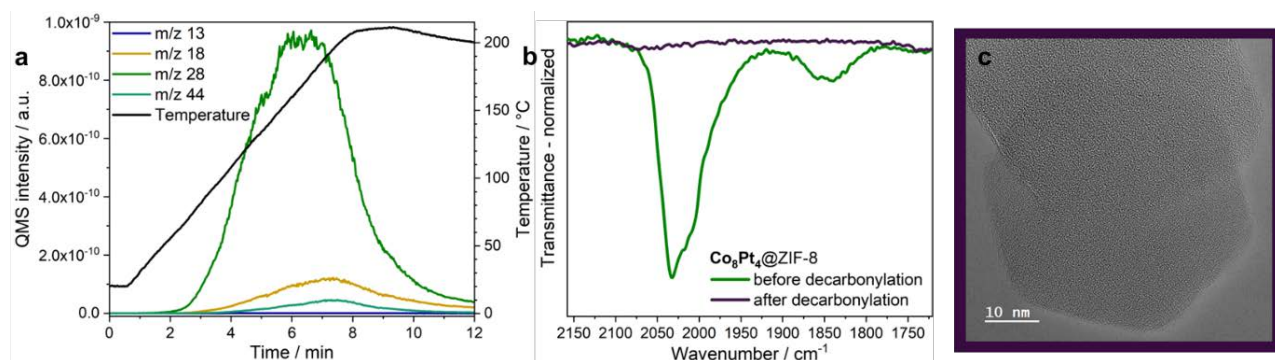


**Figure 5.** The CO removal was monitored by **a** TPD with QMS analysis of m/z 13 (CH), 18 (H<sub>2</sub>O), 28 (CO), 44 (CO<sub>2</sub>) and **b** the IR spectra visualizing the CO-removal of Co<sub>8</sub>Pt<sub>4</sub>@ZIF-8 which did not lead to distinct cluster agglomeration visible in **c** the HR-TEM image of Co<sub>8±x</sub>Pt<sub>4±y</sub>NC@ZIF-8.

In summary, Co<sub>8</sub>Pt<sub>4</sub> was found overall successfully encapsulated and confined within the ZIF-8 scaffold. Cluster recovery after MOF-embedding and acid-induced release was demonstrated. The pore-induced constraint on the cluster causes changes in the cluster's properties and the structure which has been observed for comparable systems before.<sup>60,61</sup> Furthermore, the MOF entrapment allows to remove the CO ligands without visible cluster agglomeration.

### 3 Conclusion

Experimental and computed analysis of the mechanism behind the *bottle-around-ship* embedment of eleven carbonyl-stabilized Pt(M) clusters into ZIF-8 afforded a fundamental understanding of the structure-encapsulation relationship. Cluster size and chemical composition were identified as contributing factors with large clusters preferentially locating on the ZIF-8 edge, and weak Pt-M bonds cleaving during the scaffolding procedure. Theoretical studies

further unveiled the pivotal role of the carbonyl ligand polarization on the ZIF-8 precursor attraction.

Alongside pure Pt clusters, for the first time a bimetallic carbonyl cluster, i.e., **Co<sub>8</sub>Pt<sub>4</sub>**, has been successfully embedded in ZIF-8. Here, monitoring the cluster inside the MOF matrix was met by combining e.g. HR-TEM and X-ray absorption spectroscopy revealing an overall cluster preservation. The MOF confinement was found to modulate the cluster's properties including the temperature-dependent paramagnetic behavior and the interatomic distances while MOF digestion permitted intact releasing of **Co<sub>8</sub>Pt<sub>4</sub>** demonstrating the carrier potential of ZIF-8. Further, the CO ligands were stripped off the ZIF-8-embedded **Co<sub>8</sub>Pt<sub>4</sub>** cluster without visible cluster size changes yielding accessible as well as confined clusters .

This work standouts from previous cluster-encapsulation studies investigating a lower cluster sample number and less mechanistic insights.<sup>17,19,20</sup> By studying a series of related cluster@MOF materials, the gained insights will facilitate applying clusters as catalysts, sensors or other energy-related materials. Specifically, the MOF-templated nanoparticle fabrication<sup>22</sup> is envisioned well-suited for generating defined bimetallic nanoparticles, as tailored (electro-)catalyst. Here, DFT calculations and AIMD simulations were identified as reliable tools to find suitable cluster candidates for MOF encapsulation. These findings are anticipated transferable to other host-guest systems. In combination with the gained mechanistic knowledge this study may pave the way for a more rational material design.

## ASSOCIATED CONTENT

### **Supporting Information.**

The following files are available free of charge.

The ESI includes general information about the experimental procedures and characterization methods. In addition, supplementary data for in-depth characterization is included. (file type, PDF)

## AUTHOR INFORMATION

### **Corresponding Authors**

Julien Warnan\*. Roland A. Fischer \*.

Department of Chemistry, Technical University of Munich, Lichtenbergstraße 4, 85748, Garching, Germany

E-mail: roland.fischer@tum.de, julien.warnan@tum.de

### **Author Contributions**

KLK conducted the experiments and data analysis with contributions from P (theoretical section). The PtM cluster synthesis was conducted by CC. The DFT calculations and AIMD were conducted and evaluated by WK and P. XANES and EXAFS were measured and evaluated by RK. HR-TEM, HAADF-STEM and EDX elemental mapping was conducted by MB, OT, and JM. XPS and TPD-MS were conducted and evaluated by TK. The project was conceived and designed by KLK, JW, RAF, and AG. Academic guidance and financial support was provided by

AG, SG, TL, EM, SZ, JW and RAF. The majority of manuscript writing was done by KKK and JW, supported by P, WK, and RAF. All authors have contributed to and approved the final version of this manuscript and supporting information.

## **Funding Sources**

Deutsche Bundesstiftung Umwelt (DBU)

“ARTEMIS” - TUM innovation network, Technical University of Munich funded through the German Excellence Initiative and the state of Bavaria

CzechNanoLab project LM2018110 in CEITEC Nano Research Infrastructure

Deutsche Forschungsgemeinschaft (DFG, German Research Foundation) under Germany's Excellence Strategy – EXC 2089/1 – 390776260

Swedish Research Council under contract 2018-07152, the Swedish Governmental Agency for Innovation Systems under contract 2018-04969, and Formas under contract 2019-02496.

Financial support from the German Research Foundation (DFG) within the project BA 5795/6-1

Operational Programme Research, Development and Education - European Regional Development Fund, project no. CZ.02.1.01/0.0/0.0/15\_003/0000416 of the Ministry of Education, Youth and Sports of the Czech Republic

## **Notes**

### **ACKNOWLEDGMENT**

KKK thanks the Deutsche Bundesstiftung Umwelt (DBU) for funding. KKK is grateful for proof reading by Raphael Bühler and Patrick Mollik. We thank Raphael Bühler for SQUID

measurements, Katja Rodewald for SEM measurements, and Carsten Peters for helping with the TEM imaging. KLK thanks Kathrin Weger for initial experiments and support as well as Julian Zuber, Lukas Bichlmaier, Marcel Klotz and Benedikt Kerscher for their great support in the laboratory.

The authors thanks the TUM Innovation Networks *Artificial Intelligence Powered Multifunctional Materials Design* (ARTEMIS). The HAADF-STEM measurements using TITAN microscope were performed with support of CzechNanoLab project LM2018110 in CEITEC NanoResearch Infrastructure. MB und TL acknowledge the Deutsche Forschungsgemeinschaft (DFG, German Research Foundation) under Germany's Excellence Strategy – EXC 2089/1 – 390776260 for funding. The X-ray emission spectroscopy measurements were performed on beamline ID26 at the European Synchrotron Radiation Facility (ESRF) in Grenoble, France. We acknowledge the ESRF for the provision of synchrotron radiation facilities, and we would like to thank Dr. Blanka Detlefs for assistance in measurements. The X-ray absorption spectroscopy measurements were performed on the Balder beamline of the Max IV Laboratory in Lund, Sweden. We would like to thank Dr. Konstantin Klementiev for his assistance during the measurements. Research conducted at MAX IV, a Swedish national user facility, is supported by the Swedish Research Council under contract 2018-07152, the Swedish Governmental Agency for Innovation Systems under contract 2018-04969, and Formas under contract 2019-02496. Financial support from the German Research Foundation (DFG) within the project BA 5795/6-1 is gratefully acknowledged. OT gratefully acknowledges the support by the Operational Programme Research, Development and Education - European Regional Development Fund, project no. CZ.02.1.01/0.0/0.0/15\_003/0000416 of the Ministry of Education, Youth and Sports of the Czech Republic.

## REFERENCES

- (1) Shipway, A. N.; Katz, E.; Willner, I. Nanoparticle Arrays on Surfaces for Electronic, Optical, and Sensor Applications. *Chem. Phys. Chem.* 2000, 1 (1), 18–52.
- (2) Xie, C.; Niu, Z.; Kim, D.; Li, M.; Yang, P. Surface and Interface Control in Nanoparticle Catalysis. *Chem. Rev.* 2020, 120 (2), 1184–1249.
- (3) Astruc, D. Introduction: Nanoparticles in Catalysis. *Chem. Rev.* 2020, 120 (2), 461–463.
- (4) Rück, M.; Bandarenka, A.; Calle-Vallejo, F.; Gagliardi, A. Fast identification of optimal pure platinum nanoparticle shapes and sizes for efficient oxygen electroreduction. *Nanoscale Adv.* 2019, 1 (8), 2901–2909.
- (5) Rong, H.; Ji, S.; Zhang, J.; Wang, D.; Li, Y. Synthetic strategies of supported atomic clusters for heterogeneous catalysis. *Nat. Commun.* 2020, 11 (1), 5884.
- (6) Crampton, A. S.; Rötzer, M. D.; Ridge, C. J.; Schweinberger, F. F.; Heiz, U.; Yoon, B.; Landman, U. Structure sensitivity in the nonscalable regime explored via catalysed ethylene hydrogenation on supported platinum nanoclusters. *Nat. Commun.* 2016, 7, 10389.
- (7) Du, Y.; Sheng, H.; Astruc, D.; Zhu, M. Atomically Precise Noble Metal Nanoclusters as Efficient Catalysts: A Bridge between Structure and Properties. *Chem. Rev.* 2020, 120 (2), 526–622.
- (8) Garlyyev, B.; Fichtner, J.; Piqué, O.; Schneider, O.; Bandarenka, A. S.; Calle-Vallejo, F. Revealing the nature of active sites in electrocatalysis. *Chem. Sci.* 2019, 10 (35), 8060–8075.



- (9) Baletto, F. Structural properties of sub-nanometer metallic clusters. *J. Phys.: Condens. Matter* 2019, 31 (11), 113001.
- (10) Cesari, C.; Shon, J.-H.; Zacchini, S.; Berben, L. A. Metal carbonyl clusters of groups 8-10: synthesis and catalysis. *Chem. Soc. Rev.* 2021, 50 (17), 9503–9539.
- (11) Shu, Y.; Ye, Q.; Dai, T.; Xu, Q.; Hu, X. Encapsulation of Luminescent Guests to Construct Luminescent Metal-Organic Frameworks for Chemical Sensing. *ACS Sens.* 2021, 6 (3), 641–658.
- (12) Gao, C.; Lyu, F.; Yin, Y. Encapsulated Metal Nanoparticles for Catalysis. *Chem. Rev.* 2021, 121 (2), 834–881.
- (13) Kollmannsberger, K. L.; Kronthaler, L.; Jinschek, J. R.; Fischer, R. A. Defined metal atom aggregates precisely incorporated into metal-organic frameworks. *Chem. Soc. Rev.* 2022, 51, 9933–9959.
- (14) Bennett, T. H.; Vaughn, M. D.; Davari, S. A.; Park, K.; Mukherjee, D.; Khomami, B. Jolly green MOF: confinement and photoactivation of photosystem I in a metal–organic framework. *Nanoscale Adv.* 2019, 1 (1), 94–104.
- (15) Ji, S.; Chen, Y.; Fu, Q.; Chen, Y.; Dong, J.; Chen, W.; Li, Z.; Wang, Y.; Gu, L.; He, W.; Chen, C.; Peng, Q.; Huang, Y.; Duan, X.; Wang, D.; Draxl, C.; Li, Y. Confined Pyrolysis within Metal-Organic Frameworks To Form Uniform Ru<sub>3</sub> Clusters for Efficient Oxidation of Alcohols. *J. Am. Chem. Soc.* 2017, 139 (29), 9795–9798.

- (16) Luo, Y.; Fan, S.; Yu, W.; Wu, Z.; Cullen, D. A.; Liang, C.; Shi, J.; Su, C. Fabrication of Au<sub>25</sub>(SG)<sub>18</sub> -ZIF-8 Nanocomposites: A Facile Strategy to Position Au<sub>25</sub>(SG)<sub>18</sub> Nanoclusters Inside and Outside ZIF-8. *Adv. Mater.* 2018, 30 (6), 1704576-1704576.
- (17) Sun, L.; Yun, Y.; Sheng, H.; Du, Y.; Ding, Y.; Wu, P.; Li, P.; Zhu, M. Rational encapsulation of atomically precise nanoclusters into metal–organic frameworks by electrostatic attraction for CO<sub>2</sub> conversion. *J. Mater. Chem. A* 2018, 6 (31), 15371–15376.
- (18) Kratzl, K.; Kratky, T.; Günther, S.; Tomanec, O.; Zbořil, R.; Michalička, J.; Macak, J. M.; Cokoja, M.; Fischer, R. A. Generation and Stabilization of Small Platinum Clusters Pt<sub>12±x</sub> Inside a Metal-Organic Framework. *J. Am. Chem. Soc* 2019, 141 (35), 13962–13969.
- (19) Zhu, Y.; Qiu, X.; Zhao, S.; Guo, J.; Zhang, X.; Zhao, W.; Shi, Y.; Tang, Z. Structure regulated catalytic performance of gold nanocluster-MOF nanocomposites. *Nano Res.* 2020, 13 (7), 1928–1932.
- (20) Kollmannsberger, K. L.; Weger, K.; Kratky, T.; Günther, S.; Tomanec, O.; Warnan, J.; Fischer, R. A. From phosphine-stabilised towards naked Au<sub>8</sub> clusters through ZIF-8 encapsulation. *Mol. Syst. Des. Eng.* 2021, 6 (11), 876–882.
- (21) Zheng, F.; Fan, Y.; Chen, W. Homogeneous Distribution of Pt<sub>16</sub>(C<sub>4</sub>O<sub>4</sub>SH<sub>5</sub>)<sub>26</sub> Clusters in ZIF-67 for Efficient Hydrogen Generation and Oxygen Reduction. *ACS Appl. Mater. Interfaces* 2021, 13 (32), 38170–38178.
- (22) Garlyyev, B.; Kratzl, K.; Rück, M.; Michalička, J.; Fichtner, J.; Macak, J. M.; Kratky, T.; Günther, S.; Cokoja, M.; Bandarenka, A. S.; Gagliardi, A.; Fischer, R. A. Optimizing the Size of

Platinum Nanoparticles for Enhanced Mass Activity in the Electrochemical Oxygen Reduction Reaction. *Angew. Chem.* 2019, 58 (28), 9596–9600.

(23) Feng, Y.; Xu, Y.; Liu, S.; Di Wu; Su, Z.; Chen, G.; Liu, J.; Li, G. Recent advances in enzyme immobilization based on novel porous framework materials and its applications in biosensing. *Coord. Chem. Rev.* 2022, 459, 214414.

(24) Zhang, H.; Wang, B.; Yu, X.; Li, J.; Shang, J.; Yu, J. Carbon Dots in Porous Materials: Host-Guest Synergy for Enhanced Performance. *Angew. Chem.* 2020, 59 (44), 19390–19402.

(25) Yu, R.; Kuang, X.-F.; Wu, X.-Y.; Lu, C.-Z.; Donahue, J. P. Stabilization and immobilization of polyoxometalates in porous coordination polymers through host–guest interactions. *Coord. Chem. Rev.* 2009, 253 (23-24), 2872–2890.

(26) Cases Díaz, J.; Lozano-Torres, B.; Giménez-Marqués, M. Boosting Protein Encapsulation through Lewis-Acid-Mediated Metal-Organic Framework Mineralization: Toward Effective Intracellular Delivery. *Chem. Mater.* 2022, 34 (17), 7817–7827.

(27) Femoni, C.; Iapalucci, M. C.; Longoni, G.; Zacchini, S.; Fedi, S.; Fabrizi de Biani, F. Cage Rearrangements in Dodecanuclear Co–Pt Dicarbido Clusters Promoted by Redox Reactions. *Eur. J. Inorg. Chem.* 2012, 2012 (13), 2243–2250.

(28) Cesari, C.; Berti, B.; Bortoluzzi, M.; Femoni, C.; Iapalucci, M. C.; Zacchini, S. Heterometallic Ni-Pt Chini-Type Carbonyl Clusters: An Example of Molecular Random Alloy Clusters. *Inorg. Chem.* 2021, 60 (12), 8811–8825.

(29) Cesari, C.; Berti, B.; Bortoluzzi, M.; Femoni, C.; Funaioli, T.; Vivaldi, F. M.; Iapalucci, M. C.; Zacchini, S. From M<sub>6</sub> to M<sub>12</sub>, M<sub>19</sub> and M<sub>38</sub> molecular alloy Pt-Ni carbonyl

nanoclusters: selective growth of atomically precise heterometallic nanoclusters. Dalton Trans. 2023, 52 (12), 3623–3642.

(30) Femoni, C.; Iapalucci, M. C.; Longoni, G.; Svensson, P. H.; Zanello, P.; Fabrizi de Biani, F. Synthesis and characterisation of n<sup>3</sup>-octahedral [Ni<sub>36</sub>Pd<sub>8</sub>(CO)<sub>48</sub>]<sup>6-</sup> and [Ni<sub>35</sub>Pt<sub>9</sub>(CO)<sub>48</sub>]<sup>6-</sup> clusters displaying unexpected surface segregation of Pt atoms and molecular and/or crystal substitutional Ni/Pd and Ni/Pt disorder. Chem. Eur. J. 2004, 10 (9), 2318–2326.

(31) Giuliano Longoni; Mario Manassero; and Mirella Sansoni. Synthesis and structural characterization of bimetallic Fe-Pt carbonyl clusters: their relationship with bimetallic Fe-Pd carbonyl clusters. J. Am. Chem. Soc 1980 (102), 7973–7974.

(32) Bortoluzzi, M.; Ceriotti, A.; Cesari, C.; Ciabatti, I.; Della Pergola, R.; Femoni, C.; Iapalucci, M. C.; Storione, A.; Zacchini, S. Syntheses of [Pt<sub>6</sub>(CO)<sub>8</sub>(SnCl<sub>2</sub>)(SnCl<sub>3</sub>)<sub>4</sub>]<sup>4-</sup> and [Pt<sub>6</sub>(CO)<sub>8</sub>(SnCl<sub>2</sub>)(SnCl<sub>3</sub>)<sub>2</sub>(PPh<sub>3</sub>)<sub>2</sub>]<sup>2-</sup> Platinum-Carbonyl Clusters Decorated by SnII Fragments. Eur. J. Inorg. Chem. 2016, 2016 (24), 3939–3949.

(33) Calabrese, J. C.; Dahl, L. F.; Chini, P.; Longoni, G.; Martinengo, S. Synthesis and Structural Characterization of Platinum Carbonyl Cluster Dianions, [Pt<sub>3</sub>(CO)<sub>3</sub>(μ<sub>2</sub>-CO)<sub>3</sub>]<sup>n2-</sup> (n = 2, 3, 4, 5). New Series of Inorganic Oligomers. J. Am. Chem. Soc. 1974, 96 (8), 2614–2616.

(34) Don M. Washecheck, Edward J. Wucherer, Lawrence F. Dahl, Alessandro Ceriotti, Giuliano Longoni, Mario Manassero, Mirella Sansoni, and Paolo Chini. Synthesis, structure, and stereochemical implication of the [Pt<sub>19</sub>(CO)<sub>12</sub>(μ<sub>2</sub>-CO)<sub>10</sub>]<sup>4-</sup> tetraanion: a bicapped triple-decker all-metal sandwich of idealized fivefold (D<sub>5h</sub>) geometry. J. Am. Chem. Soc. 1979, 101 (20), 6110-6112.

(35) Ceriotti, A.; Masciocchi, N.; Macchi, P.; Longoni, G. [Pt<sub>19</sub>(CO)<sub>21</sub>(NO)]<sup>3-</sup> and [Pt<sub>38</sub>(CO)<sub>44</sub>]<sup>2-</sup>: Nitrosyl Bending through Intramolecular Electron Transfer as an Intermediate Step in the Nucleation Process from Polydecker to cccp Platinum Carbonyl Clusters. *Angew. Chem. Int. Ed.* 1999, 38 (24), 3724–3727.

(36) Čolić, V.; Bandarenka, A. S. Pt Alloy Electrocatalysts for the Oxygen Reduction Reaction: From Model Surfaces to Nanostructured Systems. *ACS Catal.* 2016, 6 (8), 5378–5385.

(37) Wang, X.; Li, Z.; Qu, Y.; Yuan, T.; Wang, W.; Wu, Y.; Li, Y. Review of Metal Catalysts for Oxygen Reduction Reaction: From Nanoscale Engineering to Atomic Design. *Chem* 2019, 5 (6), 1486–1511.

(38) Lu, L. Nanoporous noble metal-based alloys: a review on synthesis and applications to electrocatalysis and electrochemical sensing. *Mikrochim. acta* 2019, 186 (9), 664.

(39) Chen, A.; Holt-Hindle, P. Platinum-based nanostructured materials: synthesis, properties, and applications. *Chem. Rev.* 2010, 110 (6), 3767–3804.

(40) Shang, L.; Dong, S.; Nienhaus, G. U. Ultra-small fluorescent metal nanoclusters: Synthesis and biological applications. *Nano Today* 2011, 6 (4), 401–418.

(41) Macchi, P. Chemical bonding in transition metal carbonyl clusters: complementary analysis of theoretical and experimental electron densities. *Coord. Chem. Rev.* 2003, 238-239, 383–412.

(42) Pan, Y.; Liu, Y.; Zeng, G.; Zhao, L.; Lai, Z. Rapid synthesis of zeolitic imidazolate framework-8 (ZIF-8) nanocrystals in an aqueous system. *Chem. Commun.* 2011, 47 (7), 2071–2073.

- (43) Troyano, J.; Carné-Sánchez, A.; Avci, C.; Imaz, I.; Maspoch, D. Colloidal metal-organic framework particles: the pioneering case of ZIF-8. *Chem. Soc. Rev.* 2019, 48 (23), 5534–5546.
- (44) Dragonetti, C.; Ceriotti, A.; Roberto, D.; Ugo, R. Surface-Mediated Organometallic Synthesis: The Role of the Oxidation State and of Ancillary Ligands in the High-Yield and Selective Syntheses of Platinum Carbonyl Dianions  $[\text{Pt}_3(\text{CO})_6]^{n-}$  ( $n = 6, 5, 4, 3$ ) by Reductive Carbonylation under Mild Conditions and in the Presence of Surface Basicity of Various Silica-Supported Pt(IV) or Pt(II) Compounds. *Organometallics* 2007, 26 (2), 310–315.
- (45) Longoni, G.; Chini, P. Synthesis and chemical characterization of platinum carbonyl dianions  $[\text{Pt}_3(\text{CO})_6]^{n-}$  ( $n = 10, 6, 5, 4, 3, 2, 1$ ). A new series of inorganic oligomers. *J. Am. Chem. Soc.* 1976, 98 (23), 7225–7231.
- (46) Yun, Y.; Sheng, H.; Bao, K.; Xu, L.; Zhang, Y.; Astruc, D.; Zhu, M. Design and Remarkable Efficiency of the Robust Sandwich Cluster Composite Nanocatalysts ZIF-8@Au<sub>25</sub>@ZIF-67. *J. Am. Chem. Soc.* 2020, 142 (9), 4126–4130.
- (47) Gross, A. F.; Sherman, E.; Vajo, J. J. Aqueous room temperature synthesis of cobalt and zinc sodalite zeolitic imidizolate frameworks. *Dalton Trans.* 2012, 41 (18), 5458–5460.
- (48) Albonetti, S.; Bonelli, R.; Epoupa Mengou, J.; Femoni, C.; Tiozzo, C.; Zacchini, S.; Trifirò, F. Gold/iron carbonyl clusters as precursors for TiO<sub>2</sub> supported catalysts. *Catal. Today* 2008, 137 (2-4), 483–488.
- (49) Esken, D.; Turner, S.; Lebedev, O. I.; van Tendeloo, G.; Fischer, R. A. Au@ZIFs: Stabilization and Encapsulation of Cavity-Size Matching Gold Clusters inside Functionalized Zeolite Imidazolate Frameworks, ZIFs. *Chem. Mater.* 2010, 22 (23), 6393–6401.

(50) Bortoluzzi, M.; Ceriotti, A.; Ciabatti, I.; Della Pergola, R.; Femoni, C.; Carmela Iapalucci, M.; Storione, A.; Zacchini, S. Platinum carbonyl clusters stabilized by Sn(II)-based fragments: syntheses and structures of  $[\text{Pt}_6(\text{CO})_6(\text{SnCl}_2)_2(\text{SnCl}_3)_4]^{4-}$ ,  $[\text{Pt}_9(\text{CO})_8(\text{SnCl}_2)_3(\text{SnCl}_3)_2(\text{Cl}_2\text{SnOCOSnCl}_2)]^{4-}$  and  $[\text{Pt}_{10}(\text{CO})_{14}\{\text{Cl}_2\text{Sn}(\text{OH})\text{SnCl}_2\}_2]^{2-}$ . Dalton Trans. 2016, 45 (12), 5001–5013.

(51) Cesari, C.; Femoni, C.; Carmela Iapalucci, M.; Zacchini, S. Molecular Fe, CO and Ni carbide carbonyl clusters and Nanoclusters. Inorg. Chim. Acta 2023, 544, 121235.

(52) Femoni, C.; Iapalucci, M. C.; Kaswalder, F.; Longoni, G.; Zacchini, S. The possible role of metal carbonyl clusters in nanoscience and nanotechnologies. Coord. Chem. Rev. 2006, 250 (11-12), 1580–1604.

(53) Lu, G.; Li, S.; Guo, Z.; Farha, O. K.; Hauser, B. G.; Qi, X.; Wang, Y.; Wang, X.; Han, S.; Liu, X.; DuChene, J. S.; Zhang, H.; Zhang, Q.; Chen, X.; Ma, J.; Loo, S. C. J.; Wei, W. D.; Yang, Y.; Hupp, J. T.; Huo, F. Imparting functionality to a metal-organic framework material by controlled nanoparticle encapsulation. Nat. Chem. 2012, 4 (4), 310–316.

(54) Zobi, F. Ligand electronic parameters as a measure of the polarization of the  $\text{C}\equiv\text{O}$  bond in  $[\text{M}(\text{CO})_x\text{Ly}]_n$  complexes and of the relative stabilization of  $[\text{M}(\text{CO})_x\text{Ly}]_n/n^+$  species. Inorg. Chem. 2010, 49 (22), 10370–10377.

(55) Michael J D’Aniello, Constance J. Carr, Michael G. Zammit. Preparation of the Carbonyl Platinum Anions,  $[\text{Pt}_3(\text{CO})_6]^{2-n}$ , ( $n = 3-5$ ). Inorg. Synth. 1989 (26), 319–323.

(56) Lim, I. H.; Schrader, W.; Schüth, F. Insights into the Molecular Assembly of Zeolitic Imidazolate Frameworks by ESI-MS. Chem. Mater. 2015, 27 (8), 3088–3095.

(57) Avanzino, S. C.; Jolly, W. L. A study of bridging and terminal carbonyl groups in transition metal complexes by x-ray photoelectron spectroscopy. *J. Am. Chem. Soc.* 1976, 98 (21), 6505–6507.

(58) Papporello, R. L.; Miró, E. E.; Zamaro, J. M. Secondary growth of ZIF-8 films onto copper-based foils. Insight into surface interactions. *Microporous Mesoporous Mat.* 2015, 211, 64–72.

(59) Liu, S.; Chen, F.; Li, S.; Peng, X.; Xiong, Y. Enhanced photocatalytic conversion of greenhouse gas CO<sub>2</sub> into solar fuels over g-C<sub>3</sub>N<sub>4</sub> nanotubes with decorated transparent ZIF-8 nanoclusters. *Appl. Catal. B* 2017, 211, 1–10.

(60) Cao, X.; Cheng, S.; You, Y.; Zhang, S.; Xian, Y. Sensitive monitoring and bioimaging intracellular highly reactive oxygen species based on gold nanoclusters@nanoscale metal-organic frameworks. *Anal. Chim. Acta.* 2019, 1092, 108–116.

(61) Xia, M.; Sui, Y.; Guo, Y.; Zhang, Y. Aggregation-induced emission enhancement of gold nanoclusters in metal-organic frameworks for highly sensitive fluorescent detection of bilirubin. *The Analyst* 2021, 146, 904–910.

(62) Femoni, C.; Iapalucci, M. C.; Longoni, G.; Wolowska, J.; Zacchini, S.; Zanello, P.; Fedi, S.; Riccò, M.; Pontiroli, D.; Mazzani, M. Magnetic behavior of odd- and even-electron metal carbonyl clusters: the case study of [Co<sub>8</sub>Pt<sub>4</sub>C<sub>2</sub>(CO)<sub>24</sub>]<sup>n-</sup> (n = 1, 2) carbide cluster. *J. Am. Chem. Soc.* 2010, 132 (9), 2919–2927.

(63) Tanaka, S.; Fujita, K.; Miyake, Y.; Miyamoto, M.; Hasegawa, Y.; Makino, T.; van der Perre, S.; Cousin Saint Remi, J.; van Assche, T.; Baron, G. V.; Denayer, J. F. M. Adsorption and



Diffusion Phenomena in Crystal Size Engineered ZIF-8 MOF. *J. Phys. Chem. C* 2015, 119 (51), 28430–28439.